Mathematical Biosciences and Engineering

MBE, 19(12): 12031–12057.
DOI: 10.3934/mbe.2022560
Received: 06 June 2022
Revised: 01 August 2022
Accepted: 08 August 2022
Published: 18 August 2022

http://www.aimspress.com/journal/MBE

Research article

Duplex PD inertial damping control paradigm for active power decoupling of grid-tied virtual synchronous generator

Sue Wang[1], Jing Li[1,*], Saleem Riaz[2], Haider Zaman[3], Pengfei Hao[1], Yiwen Luo[1], Alsharef Mohammad[4], Ahmad Aziz Al-Ahmadi[4] and NasimUllah[4,*]

[1] School of Electrical and Control Engineering, Shaanxi University of Science and Technology, Xi'an 710021, China
[2] School of Automation, Northwestern Polytechnical University, Xi'an 710072, China
[3] Electronics Engineering Department, University of Engineering and Technology Peshawar, Khyber, PakhtunKhwa, Pakistan
[4] Department of Electrical Engineering College of Engineering, TAIF University, TAIF 11099, Saudi Arabia

* **Correspondence:** Email: 446721858@qq.com, nasimullah@tu.edu.sa; Tel: +15009234029.

Abstract: The growth of distributed generation significantly reduces the synchronous generators' overall rotational inertia, causing large frequency deviation and leading to an unstable grid. Adding virtual rotational inertia using virtual synchronous generators (VSG) is a promising technique to stabilize grid frequency. Due to coupled nature of frequency and active output power in a grid-tied virtual synchronous generator (GTVSG), the simultaneous design of transient response and steady state error becomes challenging. This paper presents a duplex PD inertial damping control (DPDIDC) technique to provide active power control decoupling in GTVSG. The power verses frequency characteristics of GTVSG is analyzed emphasizing the inconsistencies between the steady-state error and transient characteristics of active output power. The two PD controllers are placed in series with the generator's inertia forward channel and feedback channel. Finally, the performance superiority of the developed control scheme is validated using a simulation based study.

Keywords: virtual synchronous generator (VSG); grid-tied virtual synchronous generator (GTVSG); duplex PD inertial damping control (DPDIDC); power-frequency response characteristics

1. Introduction

To achieve the "double carbon goal" and develop green and low-carbon energy, distributed power generation technology has become an essential component of the new energy industry [1,2]. However, grid-tied inverters realize the integration of distributed power generation with the grid, exhibiting low inertia and weak damping, which is insufficient to provide the grid system's frequency and voltage support capability. The system power and frequency may lose self-regulation capability under the condition of disturbance, which seriously threatens the operation characteristics of the new power system [3,4]. Therefore, it is crucial to control the grid-tied inverter effectively. Several strategies were proposed to control VSG technology [5,6], focusing on frequency and voltage regulation features for the synchronous generator (SG). With extra-operational characteristics, the grid-tied inverter can maintain the grid power balance and frequency stability, improving the stability and safety of grid-tied system operation [7,8].

From the parameter optimization study for the GTVSG in [9,10], the rotational inertia (represented by J) and the damping factor (represented by D) determine the output response characteristics of the active power. The larger the rotational inertia J, the longer the regulation time, raising the active power overshoot and deteriorating system stability. On the other hand, when the damping factor D is larger, the active power overshoot decreases, the damping effect becomes better, and the dynamic response slows down. However, the independently increasing D seriously affects the frequency modulation characteristics of VSG active output power, leading to poor steady-state performance [11,12]. Therefore, the unreasonable selection of parameters makes the VSG prone to active power oscillations and poor active power transient and steady-state characteristics [13].

In [14] authors investigate the transient response features of GTVSG systems and suppress the KVA output power oscillations by adjusting the inertial damping. Similarly, [15] proposes an adaptive virtual inertia control approach for SG, taking advantage of the association between frequency fluctuation and virtual inertia and adjusting the inertia to enhance the microgrid frequency's dynamic characteristics. A virtual inertia adaptive control strategy for microgrids based on an improved bang-bang control strategy is proposed in [16], which uses the tunability of virtual inertia to reduce the VSG dynamic frequency deviation and improve frequency stability. To solve the problem of large fluctuations in frequency and power caused by excessive load fluctuations, reference [17] proposes a control strategy with adaptive adjustment of rotational inertia; the control strategy improves the system damping ratio and effectively suppresses the power overshoot and oscillation during transients.

The related literature work aimed to suppress the power fluctuation and frequency oscillation and improve the power output characteristics by adaptively changing the inertia and damping factor. However, in GTVSG, there is a contradiction between the active output power's transient and steady-state performance. In order to cope with these issues, according to the relationship between the system frequency change rate and inertia damping, authors in [10,18] proposed an optimal method for designing virtual inertia and damping factor for reduction of the output power and frequency fluctuations, improves dynamic power characteristics while minimizing active power steady-state errors. In [13,19], a differential compensation link is added to the forward channel of the VSG control structure. The pole-zero position of the active closed-loop transfer function is changed by adjusting the compensation coefficient, thus, improving the dynamic performance of the active power and ensuring the output power steady-state control accuracy. For the problem of mutual influence between the primary frequency modulation characteristics and damping characteristics in VSG control, the

damping feedback link is introduced [20,21]. It achieves the decoupling of frequency regulation and damping in the steady-state case and solves the problem of the trade-off between the transient and steady-state characteristics of the VSG. In [22], a virtual damped feedforward VSG control mechanism is proposed that decouples the VSG frequency modulation characteristics from the damped power connection and enhances the steady-state features of the active output power when the grid frequency deviates. By adding a correction differential link to the VSG inertia damping characteristics at various stages, enhanced inertia damping characteristics are achieved [23].

The work presented in the literature has improved the steady-state performance of active output power, solving the contradiction between the transient and the steady-state performance of the active output power. However, when designing the parameters, there is still the problem that the damping factor affects the steady-state power accuracy and is too complicated to analyze the VSG active power output performances.

This paper proposes an active power control decoupling strategy for GTVSG based on DPDIDC. By connecting a PD control link in series with the VSG inertia forward channel and a PD control link in series with the VSG damping feedback channel, the VSG system structure is changed to optimize the performance of active output power. First of all, the power-frequency response of the GTVSG system is evaluated, and pitfalls in the transient and steady-state performance of the active output power are discovered using the GTVSG control concept. Secondly, pointing out the contradictory problems between the stability and transient features of the active output power. Then, a GTVSG, active decoupling control scheme, based on DPDIDC is proposed. The closed-loop transient and steady-state characteristics of the improved GTVSG system are analyzed. The parameter constraints of DPDIDC are given and finally, the correctness and superiority of the control scheme are verified by simulation.

2. Mathematical model of GTVSG system

The GTVSG central circuit topology is shown in Figure 1. e_{abc}, u_{abc} and i_{oabc} are the VSG three-phase circuit potential, VSG output terminal voltage, and VSG output current; i_{abc} represents the three-phase AC current flowing through inductor; $i_{c\text{-}abc}$ denotes capacitance current. The *LCL* filter is chosen to filter the inverter output harmonics, $L_{1,2}$ and $R_{1,2}$ are the filter inductor and parasitic resistance, C is the filter capacitor; L_g and R_g are the line inductor and resistance, P_{ref}, Q_{ref}, ω_o and U_N are the reference values of the active output power, reactive power, the rated values of the angular frequency and voltage; P_e and Q_e are the effective values of the VSG output active power and reactive power; θ and E_m are the phase and amplitude of the active and reactive loop output reference voltages from the VSG control algorithm.

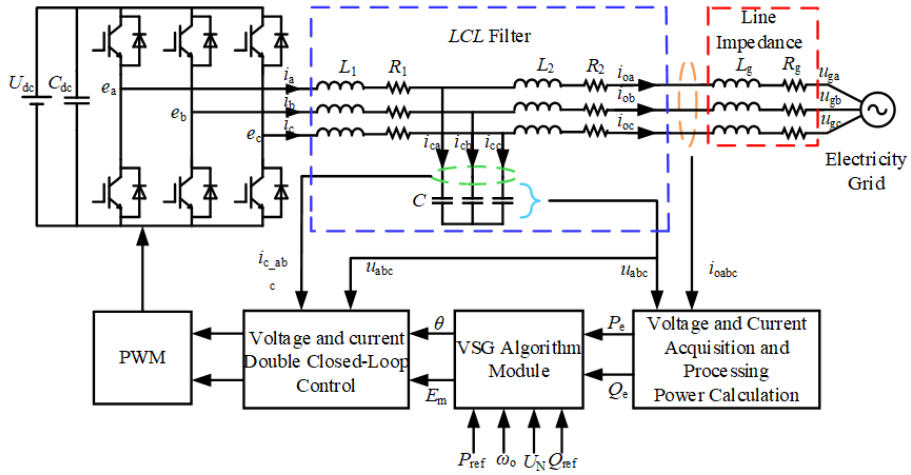

Figure 1. GTVSG central circuit topology.

According to Figure 1, the VSG system control structure mainly includes four parts: voltage and current acquisition and processing power calculation, VSG control algorithm module (active-frequency control and reactive-voltage control), voltage and current double closed-loop control and modulation strategy.

The main control principle: firstly, the power is calculated by collecting the capacitor voltage and VSG output current, and obtain the output active power, reactive power, angular frequency and voltage. Then combined with the reference value of output active power and reactive power, the rated value of angular frequency and voltage, the phase and amplitude of the output reference voltage are calculated through the active power control and reactive power control. The output voltage is controlled by voltage and current double loops, the AC voltage signal is tracked, and finally the inverter is controlled by modulating the drive signal.

2.1. Active-frequency control

Drawing on the mathematical model of synchronous generators, while simulating the inertia and damping characteristics of synchronous generators, the active power controller of VSG consists of two parts: the rotor equation of motion and the active-frequency droop control. The VSG rotor equation of motion which is obtained as follows [24]:

$$\begin{cases} J\omega_o \dfrac{d\Delta\omega}{dt} = P_m - P_e - D\left(\omega - \omega_o\right) \\ \dfrac{d\theta}{dt} = \omega \end{cases} \tag{1}$$

where J is the rotational inertia; D is the damping factor; P_m is the VSG virtual mechanical power; P_e is the VSG output active power; ω and ω_o are the effective and rated values of the VSG angular frequency; and θ is the phase angle of the VSG. VSG uses P-ω droop control to simulate the governor of the synchronous generator, to achieve the frequency modulation characteristic of the GTVSG system [9], the expression is:

$$P_m = P_{ref} - K_f\left(\omega - \omega_o\right) \tag{2}$$

where K_f is the droop factor of active power; P_{ref} is the reference value of VSG active power output.

The active-frequency control expression is obtained as:

$$\begin{cases} J\omega_o \dfrac{d\Delta\omega}{dt} = P_{ref} - P_e - \left(D + K_f\right)\left(\omega - \omega_o\right) \\ \dfrac{d\theta}{dt} = \omega \end{cases} \tag{3}$$

Therefore, the VSG active-frequency control block diagram can be obtained as shown in Figure 2.

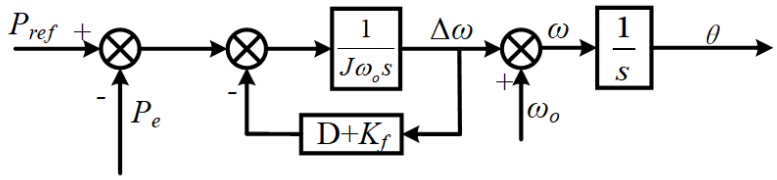

Figure 2. GTVSG active-frequency control block diagram.

The droop part of the controller implements the primary frequency regulation function, and the rotor motion characteristics realize the inertia damping support. The controller outputs the frequency of the reference voltage signal, which is integrated to form the phase angle.

2.2. Reactive-voltage control

VSG achieves output reactive power control by regulating the interrelationship between reactive power and voltage through the reactive power droop factor. So the VSG uses *Q*-*U* droop control to simulate the regulating characteristics of the synchronous generator [9], then the voltage-reactive power droop relationship equation is:

$$Q_{ref} - Q_e = K_q\left(U_N - U\right) \tag{4}$$

where E_m is the VSG output voltage; K_q denotes droop factor of KVAR; Q_e and Q_{ref} represent the actual and reference values for the VSG output; U_N is the VSG rated voltage value. The dynamic response of reactive-voltage regulation can be described using first-order inertia links.

The introduction of the $1/K_iS$ link makes the dynamic response of the excitation regulation inertial in nature and does not undergo step changes. This feature is closer to the synchronous motor in transient characteristics to prevent the power electronics from being too sensitive to reactive load changes in reactive load, causing system instability. Its reactive-voltage control expression is:

$$E_m = \frac{1}{K_i S}\left[Q_{ref} - Q_e + K_q\left(U_N - U\right)\right] \tag{5}$$

where the K_i is the factor of relevant power integration. Therefore, the VSG reactive-voltage control

block diagram can be obtained as shown in Figure 3.

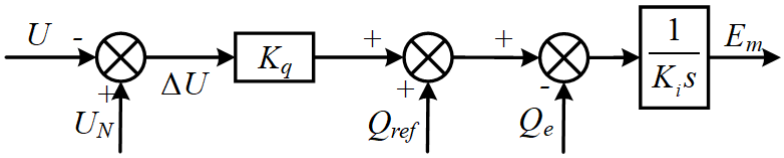

Figure 3. GTVSG reactive-voltage control block diagram.

VSG reactive-voltage control enables the inverter to have the function of voltage regulation by adjusting the voltage amplitude. After reactive-voltage control to obtain the amplitude of the reference voltage, combined with the phase obtained by active-frequency control can synthesize the reference voltage $e_{abc} = \begin{bmatrix} e_{ma} & e_{mb} & e_{mc} \end{bmatrix}^T$, the expression is:

$$\begin{cases} e_{ma} = E_m \sin\theta \\ e_{ma} = E_m \sin\left(\theta - 2/3\pi\right) \\ e_{ma} = E_m \sin\left(\theta + 2/3\pi\right) \end{cases} \tag{6}$$

2.3. Voltage and current double closed-loop control model

To maintain the output voltage stability of the virtual synchronous generator, tracking control of the voltage is required. The PI controller is used here to achieve tracking control of the voltage signal. In VSG voltage-current dual closed-loop control, the outer-loop voltage feedback is generally selected as the capacitor voltage and the inner-loop feedback is selected as the capacitor current. Figure 4 shows the VSG voltage and current double closed loop control block diagram.

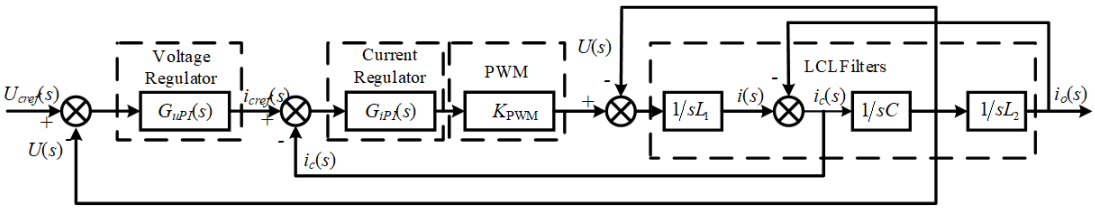

Figure 4. VSG voltage and current double closed loop control block diagram.

where U_{cref} (s) is capacitance voltage command value; G_{uPI} (s) is voltage outer loop regulator; G_{iPI} (s) is current internal loop regulator; U(s) is the VSG output capacitor voltage; i(s) is the inductor current; i_c(s) is the capacitor current; $1/sL_1$, $1/sL_2$ is the filter inductor equivalent impedance; $1/sC$ is the filter capacitor equivalent impedance; i_o(s)is the inverter output current; K_{PWM} is the inverter equivalent gain, using PWM modulation, $K_{PWM} = 1$.

As the *LCL* filter generates resonance problem, it can add damping to the system, so in the VSG

voltage and current dual-loop control, the output capacitor voltage is selected as the voltage outer-loop feedback quantity, the capacitor current is selected as the current inner-loop feedback quantity, which not only inhibits resonance, but also solves the output coupling problem. At the same time, the capacitive current inner-loop control as the feedback has more negligible output impedance, insensitive to the disturbance changes of load, and has a stronger carrying capacity [25]. Its voltage and current dual-loop both use the PI controllers to achieve the purpose of tracking and control the voltage signal.

3. GTVSG system active loop power-frequency response

According to the VSG active-frequency control expression, the power-frequency characteristic of its system is mainly reflected in the *P*-ω characteristic. Then the expression of the *P*-ω characteristic is:

$$G_{P-\omega}(s)=\frac{\omega-\omega_o}{P_{ref}-P_e}=\frac{\Delta\omega}{\Delta P_e}=\frac{1}{J\omega_o s+D+K_f} \tag{7}$$

According to Eq (7), the parameters affecting the system performance are *J*, *D*, and K_f, the power-frequency transient characteristics of the system are related to *J*, *D*, and K_f. In contrast, the power-frequency steady-state characteristics are related to D and K_f. The system can control $\Delta\omega$ by adjusting *J* and *D* to ensure the stable output of the system power-frequency output response. Since *D* and K_f have the same effect on the system characteristics, generally, the fixed value of K_f is 100% of the output power variation, and the angular frequency variation is $\Delta\omega = 1\%\omega_o$ [26,27]. Therefore, its effect on the VSG active loop power-frequency response is analyzed by varying the magnitude of *D*.

3.1. Power response characteristics

3.1.1. Stable operation features

As we can clearly see the Figure 5 shows the VSG active-power control structure and terminologies of the GTVSG closed-loop control block diagram.

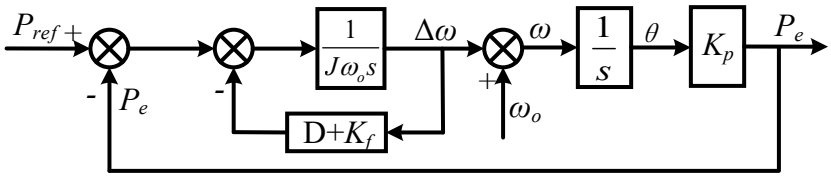

Figure 5. GTVSG active closed-loop control structure.

K_P is the gain factor of the relationship between the active output power P_e and the phase angle θ in Figure 5. According to the VSG line power transmission principle, the GTVSG system output power is:

$$\begin{cases} P_e = \dfrac{3E_m U_g}{X}\theta \\ Q_e = \dfrac{\left(3E_m - U_g\right)}{X}\cdot U_g \end{cases} \tag{8}$$

where U_g is the grid voltage amplitude, and X is the GTVSG output equivalent impedance, according to Eq (8): $K_P = 3E_m U_g / X$ [24]. The terminologies used in the above Figure 5 for the GTVSG active closed-loop control block diagram, the following expression can be drawn for a grid-connected inverter output active power P_e such that:

$$\begin{aligned} P_e &= \frac{K_P}{J\omega_o s^2 + \left(D + K_f\right)s + K_P} P_{ref} + \frac{K_P\left(J\omega_o s + D + K_f\right)}{J\omega_o s^2 + \left(D + K_f\right)s + K_P}\left(\omega_o - \omega\right) \\ &= G_{P_e - P_{ref}} P_{ref} + G_{P_e - \omega}\left(\omega_o - \omega\right) \end{aligned} \tag{9}$$

From Eq (9), the active output power P_e is affected by the VSG active power reference value and the fluctuation of the grid frequency. Thus, to recapitulate the final value theorem, the stable active power P_{eo} for a grid-connected operation can be described as follows:

$$\begin{aligned} P_{eo} &= \lim_{s\to 0}\left[G_{P_e - P_{ref}} P_{ref} + G_{P_e - \omega}\left(\omega_o - \omega\right)\right] \\ &= P_{ref} + \left(D + K_f\right)\left(\omega_o - \omega\right) \end{aligned} \tag{10}$$

According to Eq (10), the steady-state value of active output power P_{eo} is affected by two conditions: most important one is the change of active power reference value P_{ref}, while the other one is the stable power deviance $(D + K_f)$ $(\omega_o - \omega)$ due to frequency disturbance.

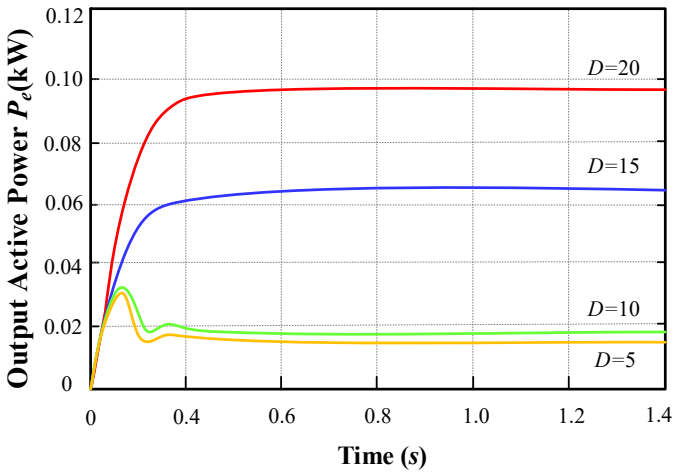

Figure 6. Step response of D on the anti-frequency disturbance capability of VSG steady-state active output power.

When the frequency fluctuations are higher, it is noticeable that the relevant steady-state error is larger. It is noticeable that parameters D and K_f mainly affect the steady-state enactment of active

power P_{eo}. While keeping K_f is fixed, the greater the damping factor D is, the higher frequency disturbance capability is. On the other hand the weaker the frequency modulation characteristics of the VSG active output power means the larger the error. Therefore, the VSG damping characteristics affect the frequency modulation capability of the VSG system, which affects the steady-state performance of the active output power. The step response of different D on the anti-frequency disturbance capability of VSG steady-state active output power is shown in Figure 6.

In Figure 6, when the active power reference value is 0, the frequency fluctuations (frequency deviation of 0.01 Hz), the damping power D seriously affects the frequency modulation accuracy of the VSG output steady-state active power. While the primary frequency modulation capability of the VSG system is very slow, and the stable output active power varies significantly with the increase of D. Hence, the steady-state performance of the active output power goes worse according.

3.1.2. Transient characteristics

The overall closed-loop small-signal transfer function may be used to study active-loop power-frequency dynamic response features of GTVSG systems [19]. In Figure 5, by expressing the relationship between the active output power and its reference value, the active output power of closed-loop small-signal transfer function is obtained as shown in Eq (11). By relating the angular frequency and the active power reference value, we can easily get the output angular frequency closed-loop small-signal transfer function as shown in Eq (12).

$$G_{P_e} = \frac{\Delta P_e}{\Delta P_{ref}} = \frac{K_P}{J\omega_o s^2 + \left(D + K_f\right)s + K_P} \tag{11}$$

$$G_{\omega} = \frac{\Delta \omega}{\Delta P_{ref}} = \frac{s}{J\omega_o s^2 + \left(D + K_f\right)s + K_P} \tag{12}$$

According to Eqs (11) and (12), the small signal transfer function for closed-loop active power is a typical second-order system. The VSG KVA power can be deduced with the help of pole placement such as:

$$s_{1,2} = \frac{-\left(D + K_f\right) \pm \sqrt{\left(D + K_f\right)^2 - 4J\omega_o K_P}}{2J\omega_o} \tag{13}$$

From Eq (13), the J and D affect the poles s_1 and s_2 of the system active closed loop. The unreasonable selection of parameters affects the distribution of zero poles, which leads to the degradation of the transient performance of the GTVSG system in the dynamic adjustment process of output active power and frequency.

According to the expression of the transfer function in Eq (11), the step response can be obtained by taking the inverse Laplace transform:

$$\Delta P_e(t)=\begin{pmatrix}1-\dfrac{1}{\sqrt{1-\dfrac{(D+K_f)^2}{4J\omega_o K_P}}}e^{-\frac{D+K_f}{2J\omega_o}t}\\ g\sin\left(\sqrt{\dfrac{K_P}{J\omega_o}}\sqrt{1-\dfrac{(D+K_f)^2}{4J\omega_o K_P}}t+\arccos\dfrac{D+K_f}{2\sqrt{J\omega_o K_P}}\right)\end{pmatrix}\Delta P_{ref}(t) \tag{14}$$

According to Eq (14), the peak time t_{pp}, regulation time t_{sp}, and the power overshoot σp% of the active step response can be expressed as:

$$\begin{cases}t_{pp}=\dfrac{2\pi J\omega_o}{\sqrt{8J\omega_o K_P-(D+K_f)^2}}\\ t_{sp_e}=\dfrac{8J\omega_o}{D+K_f}\\ \sigma_p\%=e^{-\pi\frac{D+K_f}{\sqrt{4J\omega_o K_P-(D+K_f)^2}}}\end{cases} \tag{15}$$

where above expressions demonstrate that the t_{pp}, t_{sp}, and σ_p% in Eq (15), a graph of the relationship between the transient performance for an active power and the parameters J, D are drawn according to simulation. Furthermore we have analyzed the effects of J and D on the transient performance index. The variation trend of active output power transient performance index with different J and D can be seen in the following two figures (see Figures 7 and 8(a)–(c)).

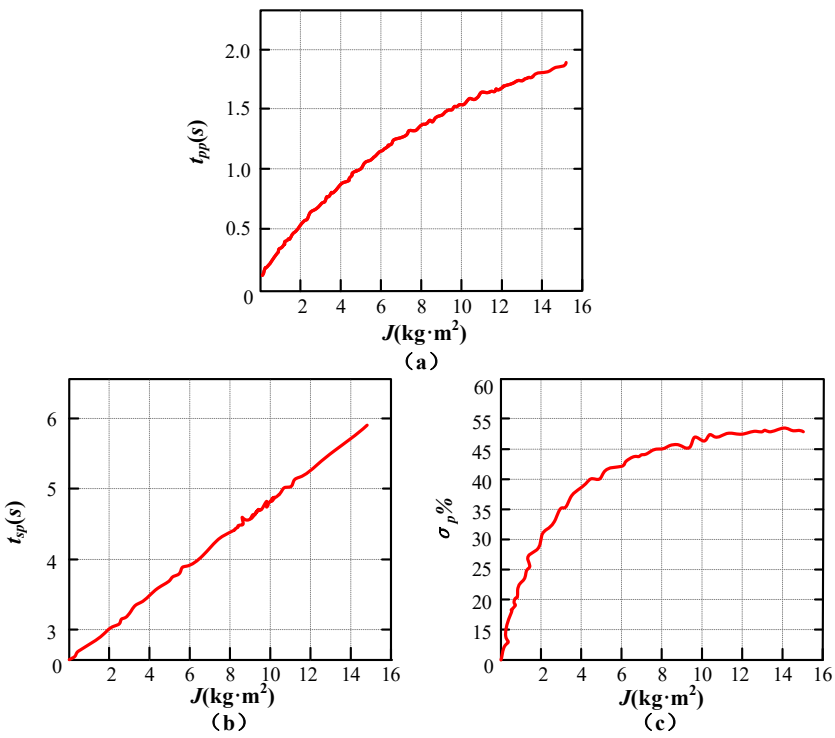

Figure 7. Variation trend of active output power transient performance index with different J.

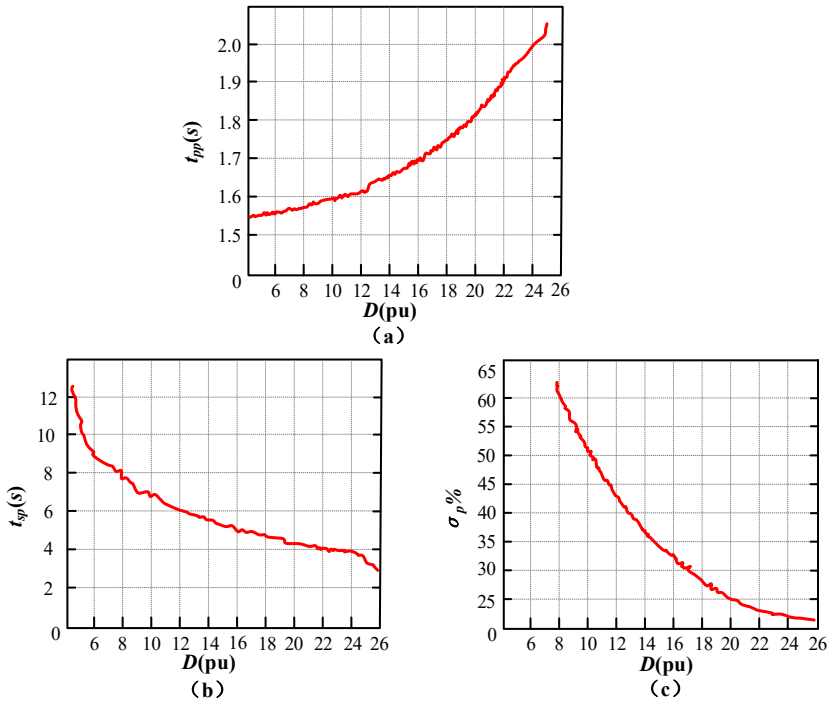

Figure 8. Variation trend of active output power transient performance index with different *D*.

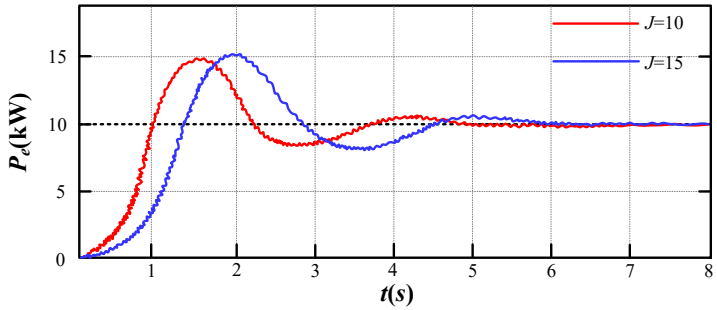

(a) Active power step response with different *J*

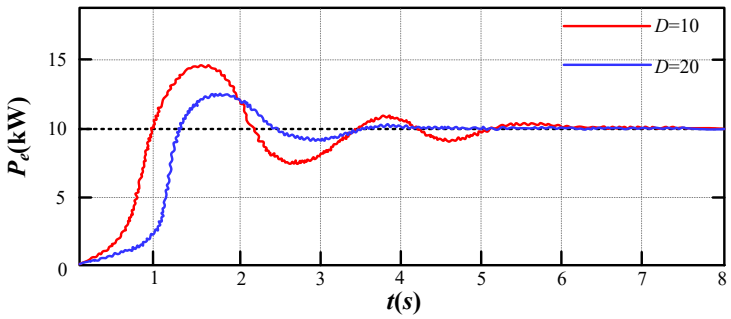

(b) Active power step response with different *D*

Figure 9. Step response of active power with different *J* and *D*.

Figures 7 and show that when *J* is larger, the damping ratio of the system is smaller, the peak time

t_{pp}, regulation time t_{sp} and overshoot σ_p% increase, the power response slows down, and the dynamic performance and stability become worse; When D is larger, the damping ratio of the system gradually increases, the peak time t_{pp} of active power increases, the regulation time t_{sp} and overshoot σ_p% decrease, and the damping effect becomes better, the power oscillation slows down, the dynamic response slows down, and the stability becomes better.

Next, the transient performance of the system affected by J and D is simulated to verify the correctness of the above theoretical analysis. Firstly, when the active power reference value is 10kW, observe the effect of J and D on the active output power step response. The step response of active power with different J and D is shown in Figure 9.

Figure 9 shows that when J increases, the peak time observed from step response grows from 1.5 to 1.8 s, the regulation time increases from 4.8 to 5.7 s, and the power overshoot increases from 44 to 53%. When D increases, the peak time of active step response increases from 1.6 to 1.8 s, the regulation time decreases from 6.3 to 4.3 s, and the power overshoot decreases from 54 to 25%. The simulation results produced are in line with the theoretical results, verifying the variation trend of active output power transient performance index with different J and D described in this paper. The comparison of the system power transient performance indicators is shown in Table 1.

Table 1 The comparison of the system power transient performance indicators.

Transient performance indicators		t_{pp} (s)	t_{sp} (s)	σ_p%
D constant	$J = 10$	1.5	4.8	44
	$J = 15$	1.8	5.7	53
J constant	$D = 10$	1.6	6.3	54
	$D = 20$	1.8	4.3	25

3.2. Frequency response characteristics

Similarly, take the inverse Laplace transform of Eq (12), and obtain the unit step response of frequency as:

$$\Delta\omega(t) = \begin{pmatrix} \left(\sqrt{\frac{K_P}{J\omega_o}} \Big/ \sqrt{1-\frac{\left(D+K_f\right)^2}{4J\omega_o K_P}}\, e^{-\frac{D+K_f}{2J\omega_o}t}\right) \\ \text{gsin}\left(\sqrt{\frac{K_P}{J\omega_o}}\sqrt{1-\frac{\left(D+K_f\right)^2}{4J\omega_o K_P}}\,t\right) \end{pmatrix} \Delta P_{ref}(t) \tag{16}$$

According to Eq (16), the peak time $t_{p\omega}$, regulation time $t_{s\omega}$ and power overshoot σ_ω% of the system frequency step response can be expressed as:

$$\begin{cases} t_{p\omega} = \dfrac{2J\omega_o K_P \arctan \dfrac{\sqrt{4J\omega_o K_P - \left(D+K_f\right)^2}}{D+K_f}}{\sqrt{4J\omega_o K_P - \left(D+K_f\right)^2}} \\ t_{s\omega} = \dfrac{8J\omega_o}{D+K_f} \\ \sigma_\omega\% = \sqrt{\dfrac{4K_P}{J\omega_o}} e^{-\pi \frac{D+K_f}{\sqrt{4J\omega_o K_P - \left(D+K_f\right)^2}} \arctan \frac{\sqrt{4J\omega_o K_P - \left(D+K_f\right)^2}}{D+K_f}} \end{cases} \tag{17}$$

Similarly, according to the expressions of $t_{p\omega}$, $t_{s\omega}$ and σ_ω% in Eq (17), a graph of the relationship between the transient performance index of the system angular frequency and J, D is drawn by simulation. Also we have analyzed the effects of J and D on the transient performance index of the angular frequency. The variation trend of the frequency transient performance index with different J and D is shown in Figures 10 and 11(a)–(c).

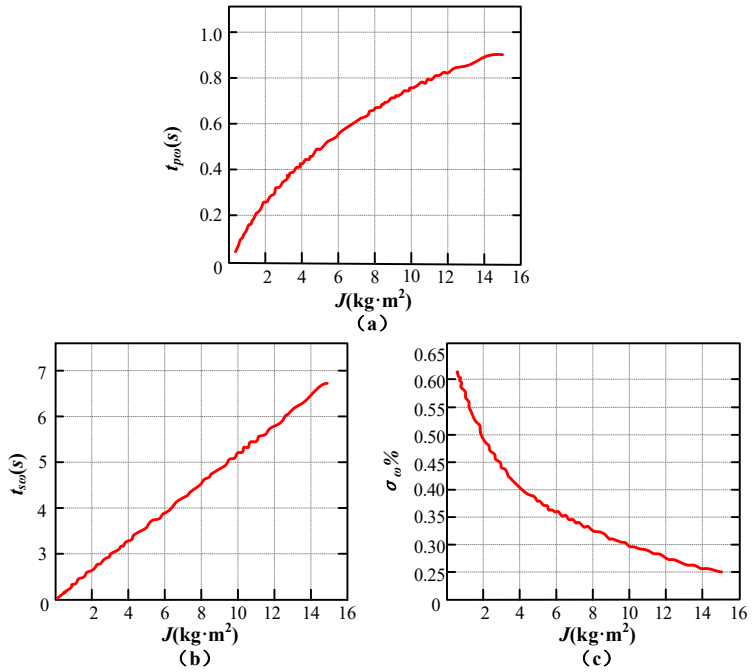

Figure 10. Variation trend of the frequency transient performance index with different J.

Figures 10 and 11 show that J can suppress the frequency variation and determines the oscillation frequency in the active output power response. When J is larger, the peak time $t_{p\omega}$ and regulation time $t_{s\omega}$ lengthen, the overshoot σ_p% decreases, and the system frequency oscillation time is too long, which is not conducive to system stability; D can reduce the amount of frequency deviation and determine the active power response oscillation decay rate. When D is larger, the peak time $t_{p\omega}$, regulation time $t_{s\omega}$ and overshoot σ_ω% decrease, and the dynamic performance becomes better.

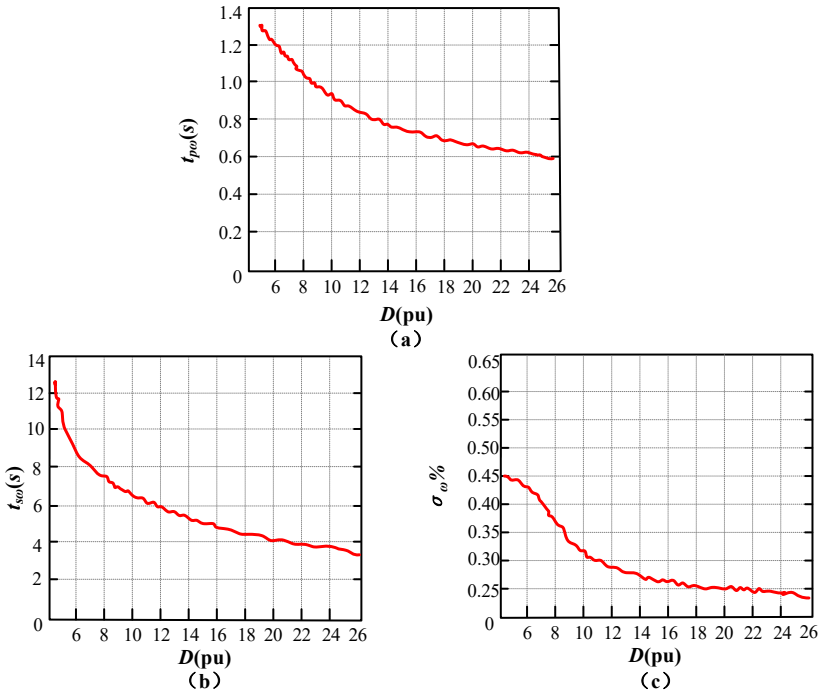

Figure 11. Variation trend of the frequency transient performance index with different *D*.

When the system frequency rating is 50 Hz, observe the effect of *J* and *D* on the output frequency step response. The step response of frequency with different *J* and *D* is shown in Figure 12.

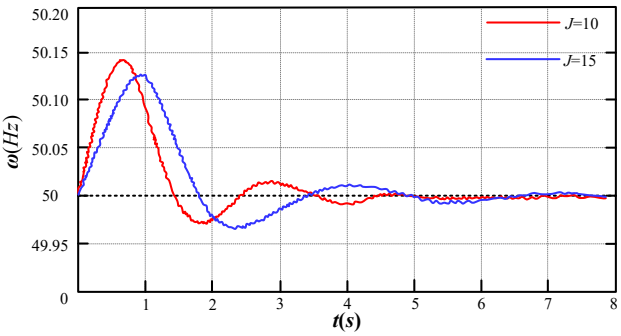

(a) The frequency step response with different *J*

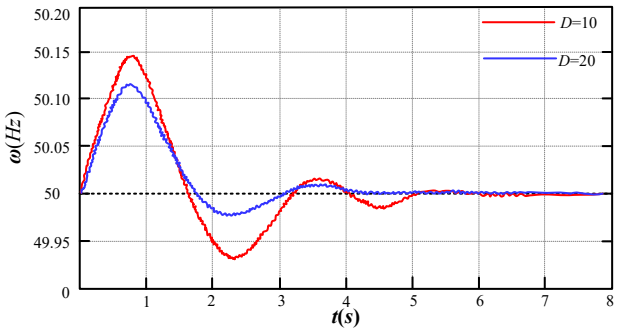

(b) The frequency step response with different *D*

Figure 12. Step response of frequency with different *J* and *D*.

Table 2 The comparison of the system frequency transient performance indicators.

Transient performance indicators		t_{pp} (s)	t_{sp} (s)	σ_p%
D constant	$J = 10$	0.7	5.2	0.30
	$J = 15$	0.9	6.3	0.25
J constant	$D = 10$	0.9	6.3	0.30
	$D = 20$	0.7	4.4	0.23

Figure 12 shows that when *J* increases, the peak time of the frequency step response increases from 0.7 to 0.9 s, the regulation time increases from 5.2 to 6.3 s, and the frequency overshoot decreases from 0.30 to 0.25%. When *D* increases, the peak time of the frequency step response decreases from 0.9 to 0.7 s, the regulation time decreases from 6.3 to 4.4 s, and the frequency overshoot decreases from 0.3 to 0.23%. The simulation results are consistent with the theoretical analysis results, which verifies the variation trend of the frequency transient performance index with different *J* and *D* described in this paper. The comparison of the system frequency transient performance indicators is shown in Table 2.

According to the analysis of the system active loop power-frequency response in Sections 3.1 and 3.2. It is obvious that the choice of *J* and *D for the output active power* has a great influence on the characteristics response, when VSG system is connected to grid. In GTVSG control strategy has a contradiction in the optimal choice of parameters for the regulation of the transient and steady-state features of the power (KVA). While the transient response of active power and frequency is associated with both *J* and *D*. We can easily chose smaller *J* and larger *D* which is advantageous to the transient characteristics of the system. However, the steady-state response of active power is only linked to D. When *D* increases, it means the rise in frequency deviation, the GTVSG steady-state power error increases, which is not conducive to frequency steady-state regulation, and the active output power steady-state performance deteriorates. In summary, the selection of *J* and *D* cannot satisfy the requirements of the transient as well as steady-state characteristics of the active output power, so the structure of the VSG needs to be reasonably designed to improve and satisfy the performance requirements of the system. Therefore, to address these issues, the paper mainly introduces PD control to the inertia damping channel, which varies the GTVSG closed-loop construction. That is decoupling control on the transient and stable performance of GTVSG system.

4. GTVSG control strategy based on duplex PD control inertia damping

4.1. PD control link

According to the classical control theory, PD control and feedback control are commonly used to improve the performance of second-order systems. PD control produces a correction effect in advance of the position error of the output signal, so as to achieve the purpose of improving the system performance. It is equivalent to increasing the system damping, adding a closed-loop zero to the system, so that the system step response overshoot is reduced and the setting time is shortened, and does not affect the constant steady-state error of the system. Due to the adoption of differential terms, larger open-loop gain is allowed to be selected, so the steady-state error can be reduced under ensure dynamic

performance conditions [28]. Therefore, PD control is introduced in the VSG inertia forward channel and the damping feedback channel respectively. The VSG control block diagram based on dual PD control inertia damping is shown in Figure 13.

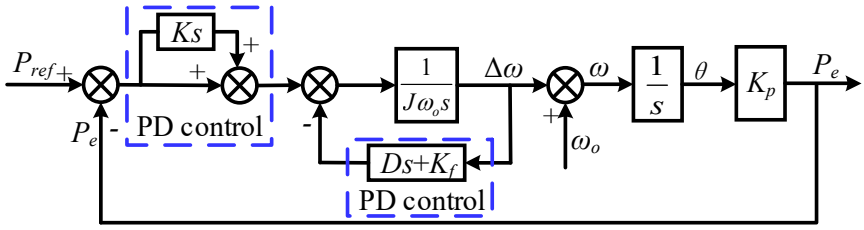

Figure 13. VSG control block diagram based on dual PD control inertia damping.

According to Figure 13, the expression of GTVSG active output power $P_{e\mathrm{mod}}$ based on duplex PD control inertia damping is:

$$\begin{aligned} P_{e\mathrm{mod}} &= \frac{K_P + KK_P s}{\left(J\omega_o + D\right)s^2 + \left(K_f + KK_P\right)s + K_P} P_{ref} \\ &+ \frac{K_P\left(J\omega_o + D\right)s + K_f K_P}{\left(J\omega_o + D\right)s^2 + \left(K_f + KK_P\right)s + K_P}\left(\omega_o - \omega\right) \end{aligned} \tag{18}$$

In a view of Eq (18), the GTVSG system with dual PD control enhances a closed-loop response. The zero pole placement could be adjusted and controlled by the differential gain K, thus satisfying the requirements of the system transient characteristics index.

4.1.1. Effect of inertia damping parameters of dual PD control on the GTVSG active power steady-state characteristics

According to the final value theorem, the active output power $P_{eo\mathrm{mod}}$ expression of the GTVSG system in the steady-state case is:

$$P_{eo\mathrm{mod}} = P_{ref} + K_f\left(\omega_o - \omega\right) \tag{19}$$

According to Eq (19), the active output power steady-state value $P_{eo\mathrm{mod}}$ consists of active power reference value P_{ref} and primary frequency modulation link K_f (ω_o-ω). The VSG damping characteristics do not affect the primary frequency modulation characteristics of the active power control. There is no steady-state error caused by D during GTVSG steady-state operation, and improves the stable performance of the KVA power. Without introducing other parameters, PD control is added to the feedback channel to improve the steady-state performance of the active power. Based on the inertia damping control structure with dual PD control, the step response of D on the improved VSG steady-state output active power against frequency disturbance is obtained as shown in Figure 14.

Figure 14 shows that, after adding the PD control, observing the influence of D on the improved GTVSG steady-state output active power. Similarly, when the active power reference value is set to 0, after the VSG inertia damping control structure changes, when the frequency fluctuates, the output of

the steady output power changes little. The D has no effect of a frequency regulation for the VSG output steady-state output power. We know that the output power is dynamically adjusted with the help of frequency regulation characteristics. Also consecutively reaching to a fixed value and then steady-state output, which can realize the steady-state operation of the active power. Simultaneously, with the increase of D, the active power oscillation slows down and improves the system transient features.

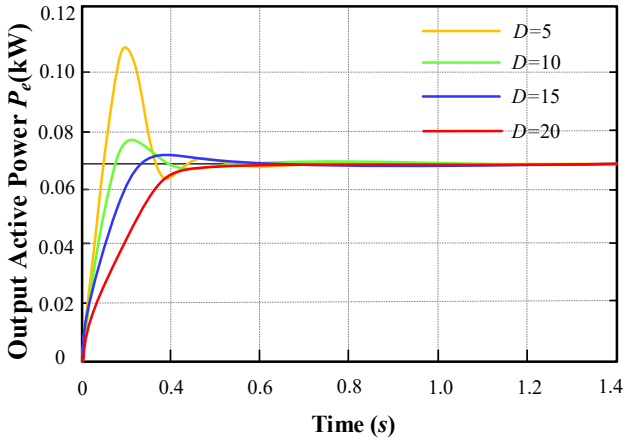

Figure 14. Step response of D on the improved VSG steady-state output active power against frequency disturbance.

4.1.2. Effect of inertia damping parameters of dual PD control on the GTVSG active power transient characteristics

We can easily adjust the pole placement with the choice of K value of grid-connected active power that can be changed to improve the transient characteristics of grid-connected active power. Referring to the system simulation parameters in Table 3, when J = 2, D = 15 and K = 0–0.2, the GTVSG active closed-loop zero-pole placement is obtained which is illustrated in Figure 15.

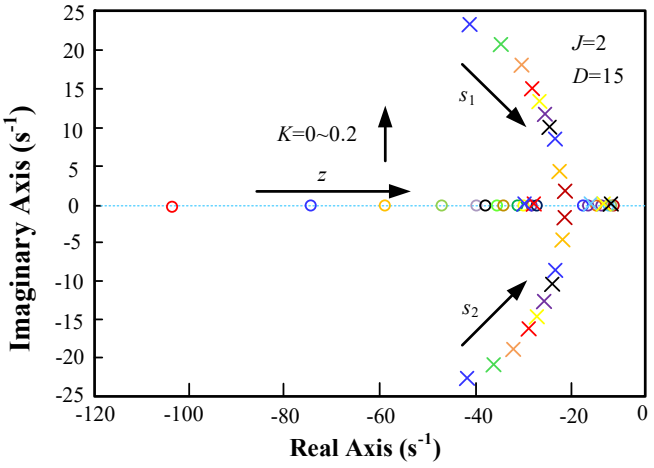

Figure 15. Improved GTVSG active closed-loop zero-pole distribution with increasing K.

From Figure 15, as the K increases further, the zero z of the closed-loop system transfer function rapidly approaches the imaginary axis. The two poles s_1 and s_2 approach the imaginary axis, gradually approach the real axis and meet at the real axis. The system enters the over-damping state, the damping ratio increases, the power oscillation amplitude decreases, and the overshoot decreases. Therefore, the added differential term has the same effect as D. The transient response of the system can be improved by increasing the K without affecting the steady-state evaluation of the system.

By improving the GTVSG active link loop, it is found that the selection of J and D can take into account the requirements of both the transient and steady-state characteristics of the active output power. Simultaneously, dual PD control increases the selection range of parameters of the inertial damping. The choice of the K has an essential impact on the active power performance. By adjusting the zero-pole position of the grid-connected system, the overall characteristics of the system are improved, so as to realize the decoupling control of the steady-state and transient characteristics of the active power.

4.2. Parameter design of dual PD control

According to Eq (18), based on the dual PD control inertia damping, the natural oscillation frequency ω_{nmod} and damping ratio ζ_{mod} of the GTVSG transfer function can be obtained:

$$\begin{cases} \omega_{n\mathrm{mod}} = \sqrt{\dfrac{K_P}{J\omega_o + D}} \\ \zeta_{\mathrm{mod}} = \dfrac{KK_P + K_f}{2\sqrt{K_P\left(J\omega_o + D\right)}} \end{cases} \tag{20}$$

In Eq (20), dynamic adjustment of K and J can effectively realize the damping regulation of VSG active closed-loop system. Increasing the K can raise the damping ratio of the system and satisfy the constraints of stability margin, overshoot and damping ratio.

1) Stability margin

The open-loop transfer function $G_{mod}(s)$ of the active power control loop based on the dual PD control is:

$$G_{\mathrm{mod}}\left(s\right) = \frac{KK_P s + K_P}{\left(J\omega_o + D\right)s^2 + K_f s} \tag{21}$$

Convert Eq (21) to a standard Type I system:

$$G_{\mathrm{mod}}\left(s\right) = \frac{K_P / K_f\left(Ks + 1\right)}{s\left(\dfrac{J\omega_o + D}{K_f}s + 1\right)} \tag{22}$$

when the open-loop gain of the system is $H = K_P / K_f$ and the time constant is $T = (J\omega_o + D) / K_f$, then Eq (22) can be transformed into:

$$G_{\mathrm{mod}}(s)=\frac{H(Ks+1)}{s(Ts+1)} \tag{23}$$

According to Eq (23), the open-loop frequency characteristics of the system can be obtained:

$$\begin{cases} G_{\mathrm{mod}}(j\omega)=\dfrac{H(j\omega K+1)}{j\omega(j\omega T+1)} \\ A(\omega)=\dfrac{H\sqrt{(\omega K)^2+1}}{\omega\sqrt{(\omega T)^2+1}} \\ \varphi(\omega)=-90^{\circ}+\arctg\omega K-\arctg\omega T \end{cases} \tag{24}$$

where $A(\omega)$ is the amplitude and $\varphi(\omega)$ is the phase angle. According to classical control theory, the stability of a system in the frequency domain can be measured in terms of stability margins (phase angle margin γ and amplitude margin h) [28]. Thus the phase angle margin γ and amplitude margin h can be expressed as:

$$\begin{cases} h=\dfrac{1}{A(\omega_c)}=+\infty \\ \gamma=180^{\circ}+\varphi(\omega_c)=90^{\circ}+\arctg\omega_c K-\arctg\omega_c T \end{cases} \tag{25}$$

where ω_c is the cut-off frequency, the phase angle margin γ becomes larger with the increase of the K, which is beneficial to the system's stability. The cut-off frequency ω_c of the system:

$$A(\omega_c)=\frac{H\sqrt{(\omega_c K)^2+1}}{\omega_c\sqrt{(\omega_c T)^2+1}}=1 \tag{26}$$

Equation (26) can be solved as follows:

$$\omega_c=\frac{\sqrt{(HK)^2+1+\sqrt{(2HT)^2+\left(1-(HK)^2\right)^2}}}{\sqrt{2}T} \tag{27}$$

In Eq (27), $d\omega_c / dK < 0$, so the system cut-off frequency decreases with the increase of the K. The reduction of the system cut-off frequency improves the system's ability to suppress frequency oscillations and improves the stable response of the KVA power. To obtain satisfactory performance, the phase angle margin γ and amplitude margin h should satisfy the following conditions:

$$\begin{cases} 30^{\circ}\le\gamma\le 60^{\circ} \\ h\ge 10dB \end{cases} \tag{28}$$

The value range of K can be obtained as:

$$\begin{cases} h = \dfrac{1}{A(\omega_c)} = +\infty \geq 10dB \\ \dfrac{J\omega_o + D - \sqrt{3}K_f}{\omega_c\left(\sqrt{3}(J\omega_o + D) + K_f\right)} \leq K \leq \dfrac{3(J\omega_o + D) - \sqrt{3}K_f}{\omega_c\left(\sqrt{3}(J\omega_o + D) + 3K_f\right)} \end{cases} \tag{29}$$

2) Damping ratio

When designing the PD control system, appropriately select a higher open-loop gain to not only improve the system transient characteristics, but also compensate for the loss of steady-state error. To satisfy the transient performance index with moderate overshoot and short setting time, the damping ratio ζ_{mod} should fulfill the following conditions:

$$0.6 \leq \zeta_{\text{mod}} = \frac{KK_P + K_f}{2\sqrt{K_P(J\omega_o + D)}} \leq 0.8 \tag{30}$$

Therefore, according to the system constraints, the value range of K and the corresponding parameters, the range of K and J are obtained as:

$$\begin{cases} 0.01 \leq K \leq 0.2 \\ 0.2 \leq J \leq 15 \end{cases} \tag{31}$$

5. Simulation verification

We can testify the rationality and superiority of the GTVSG system with dual PD control inertia damping proposed in the paper by using Matlab/Simulink. We have to build the GTVSG central circuit topology and control simulation model, where the system central circuit and control parameters are shown in Table 3.

Table 3. Parameters of the system for simulation.

Parameters	Value	Parameters	Value
DC voltage U_{dc}	800 V	Line inductors L_g	0.2 mH
Rated voltage U_N	311 V	Line resistance R_g	0.1 Ω
Grid voltage U_g	311 V	Rotational inertia J	6 kg·m^2
Rated frequency f_o	50 Hz	Damping factor D	20
Filter inductors L_1	5 mH	Active droop K_f	20
Filter inductors L_2	5 mH	Reactive droop K_q	30
Filter capacitor C	20 μF	Reactive power integration K_i	50
Filter resistors R_1	0.01 Ω	Active power reference P_{ref}	10 kW
Filter resistors R_2	0.01 Ω	Reactive power reference Q_{ref}	0 Var

To verify the correctness of the control scheme, the effects of D and K on the transient and steady-state performance of the GTVSG active power based on dual PD control are analyzed by simulation. In analyzing the active output power response of the GTVSG system under disturbance, this paper follows two cases: (i) the step response change of VSG output power and output frequency when the

active power reference value changes abruptly; (ii) the step change of VSG active output power when the grid frequency changes abruptly.

5.1. System performance analysis when the active power reference value changes abruptly in grid-connected mode

Under the VSG grid-connection, the active power reference value P_{ref} is 10 kW. While the reference value P_{ref} rises from 10 kW to 20 kW at 0.5 s. It can easily observed that the active output power response of the GTVSG system in four cases (J = 5, D = 0; J = 5, D = 20; J = 5, D = 0, K = 0.05; J = 5, D = 20, K = 0.05) is different. The simulation waveform diagram in Figure 16, the corresponding simulation waveform diagram of output frequency in Figure 17.

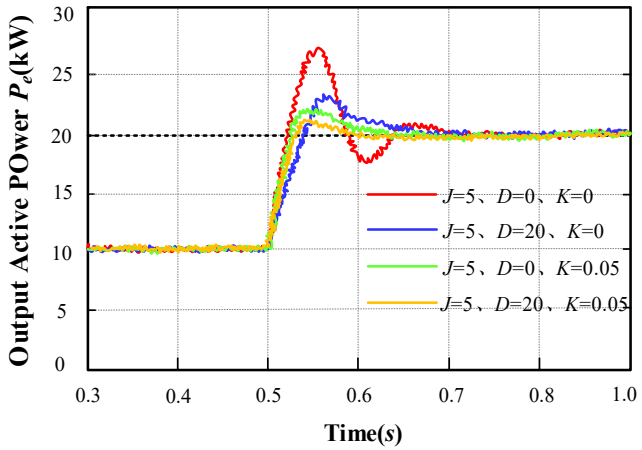

Figure 16. Simulation waveform of VSG active output power under the sudden change of reference power.

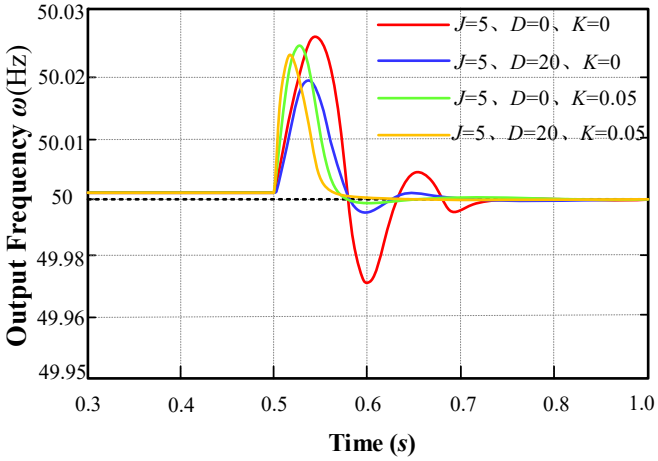

Figure 17. Simulation waveform of VSG output frequency under the sudden change of reference power.

In Figures 16 and 17, when the active power reference value increases, the VSG active power and frequency will step up. After dynamic adjustment, the active power output reaches the reference value and the frequency returns to the rated operating state, which is aligned with the grid frequency. Through the comparison of the four cases, it is found that with the increase of D, the transient performance of the system output power and frequency is better, the peak of active power fluctuation becomes smaller, the time to reach the steady-state is shorter, and the power oscillation is reduced, which helps to improve the transient performance of the system output response. With the dual PD control strategy and the introduction of K, the active power changes smoothly, which vastly reduces the overshoot and regulation time of the system, accelerates the dynamic response, and enters the stable state quickly. At the same time, K helps to improve the frequency modulation characteristics of the system, and the transient performance of the output power and frequency also is greatly improved.

5.2. System performance analysis when grid frequency changes abruptly in grid-connected mode

In Figures 18 and 19, under the VSG grid connection, the simulation waveform of VSG active output power when D and K are adjusted for a 0.05 Hz increase in grid frequency at 0.4 s.

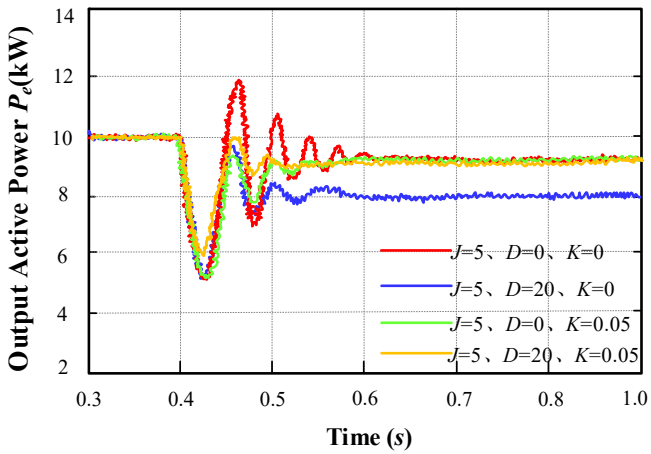

Figure 18. Simulation waveform of VSG active output power under sudden change of grid frequency.

In Figure 18, when D increases, reducing the power oscillation, because it affects the frequency modulation characteristics of the power, the active output power is lower than the regulated steady-state value, which generates a steady-state error and affects the steady-state performance of the VSG active power. After adopting the inertia damping control strategy with dual PD control, the output power is consistent with the steady-state power when reaching the steady -state, and the active power steady-state error is 0. Meanwhile, the power has no oscillation, the regulation time and overshoot are reduced, and the system soon enters the steady-state. Therefore, the inertia damping control strategy based on dual PD control not only eliminates the steady-state error, but also improves the steady-state performance of VSG active power as well as enhances the transient performance of GTVSG active power.

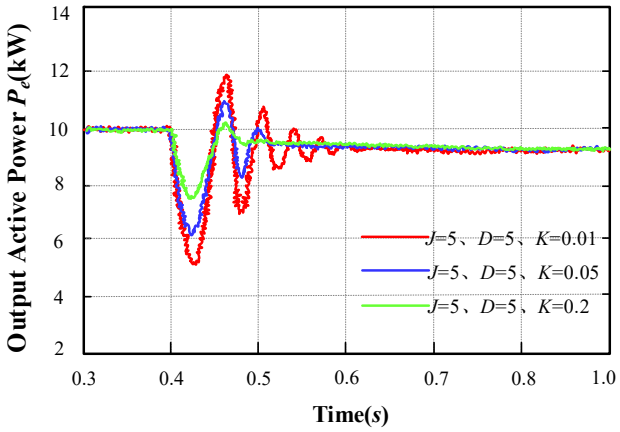

Figure 19. Simulation waveform of VSG active output power under grid frequency mutation with different *K*.

The simulation waveform of VSG active output power under grid frequency mutation with different *K* in Figure 19. By comparison, it is found that when the *K* is increased in a particular range, it not only does not disturb the stable response of GTVSG active power, but also inhibits the power oscillation. The active power overshoot and regulation time are reduced, it quickly enters stability, speeding up the response, and the transitory performance of VSG active power is greatly improved.

5.3. Comparative analysis of two control strategies

The power response performance of the system is compared between the differential compensation virtual inertia control strategy and the dual PD inertia damping control strategy to verify the superiority of the proposed control method. The comparison charts of the simulation results are shown in Figures 20–22.

1) Comparison of system transient performance

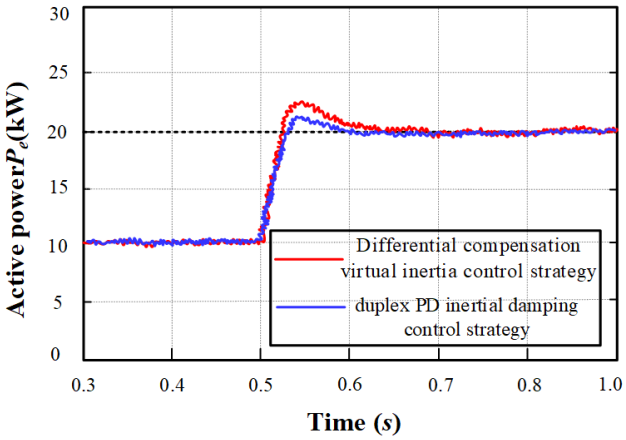

Figure 20. System output power waveforms of the two control schemes.

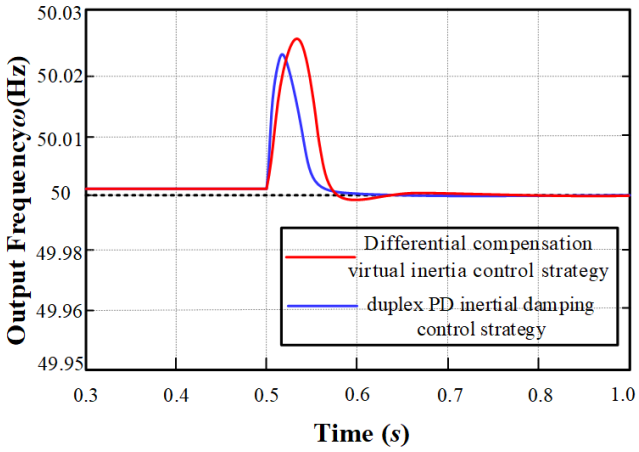

Figure 21. System output frequency waveforms of the two control schemes.

The comparison shows that after adding D, the transient performance of the system output power and frequency is better, the peak of active power fluctuation becomes smaller, the time to reach the steady state is shorter, and the power oscillation is reduced, which helps to improve the transient performance of the system output response. Therefore, the dual PD control strategy of adding D and K is more helpful to improve the frequency modulation characteristics of the system, and the transient performance of the system output power and frequency is greatly improved.

2) Comparison of system steady state performance

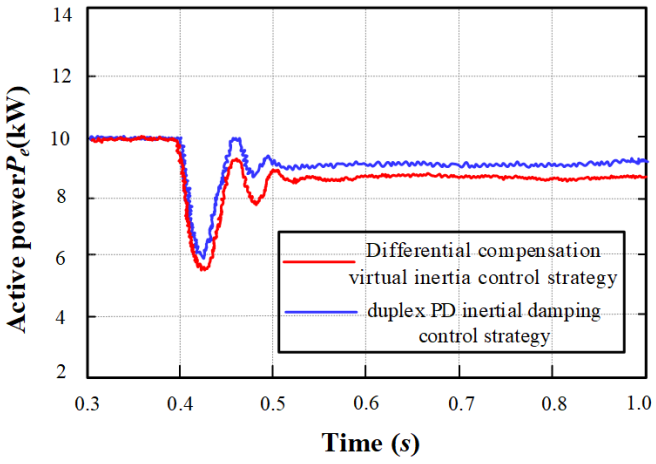

Figure 22. System output power waveforms of the two control schemes.

The comparison shows that the system output active power of differential compensation virtual inertia control strategy still has steady-state error, which affects the steady-state performance of VSG active power. After adopting the inertia damping control strategy with dual PD control, the output power is consistent with the steady-state power when reaching the steady-state, and the active power steady-state error is 0. The steady-state performance of VSG active power is greatly improved.

6. Conclusions

This paper presented a decoupling control for GTVSG founded on DPDIDC, which solves stability and transient response control problems. The theoretical analysis and simulation results show that: 1) The smaller J and the larger D are beneficial to the transient characteristics of the system. Still, too large D will increase the frequency deviation, GTVSG steady-state power error increases, and the active output power steady-state performance deteriorates. The selection of J and D is contradictory to the optimal control of active power transient and steady-state characteristics. Thus it cannot satisfy the requirements of active output power transient characteristics and steady-state characteristics simultaneously. 2) Using the proposed control strategy, the VSG inertia forward channel and the damping feedback channel are connected with PD control. With fewer parameter variables introduced, changing the structure of the GTVSG system eliminates the steady-state error in power and improves the transient characteristics of the system in both frequency and power. 3) The parameters are optimized according to the performance index requirements of the dual PD control active output power, obtaining the constraints on the parameters and the range of values.

Acknowledgements

This research work was supported by Taif University Researchers Supporting Project number (TURSP-2020/144), Taif University, Taif, Saudi Arabia.

Conflicts of interest

The authors declare there is no conflict of interest.

References

1. C. Hepburn, Y. Qi, N. Stern, B. Ward, X. Chun, D. Zenghelis, Towards carbon neutrality and China's 14th Five-Year Plan: clean energy transition, sustainable urban development, and investment priorities, *Environ. Sci. Ecotechnol.*, **8** (2021), 100–130. https://doi.org/10.1016/J.ESE.2021.100130
2. Q. C. Zhong, T. Holnick, *Control of Power Inverters in Renewable Energy and Smart Grid Integration*, John Wiley & Sons, 2012. https://doi.org/10.1002/9781118481806
3. L. Z. Yao, B. Yang, H. F. Cui, J. Zhuang, J. Ye, J. Xue, Challenges and progresses of energy storage technology and its application in power systems, *J. Mod. Power Syst. Clean Energy*, **4** (2016), 519–528. https://doi.org/10.1007/s40565-016-0248-x
4. Y. W. Wang, B. Y. Liu, S. X. Duan, Transient performance comparison of modified VSG controlled grid-tied converter, in *2019 IEEE Applied Power Electronics Conference and Exposition (APEC)*, IEEE, (2019), 3300–3303. https://doi.org/10.1109/APEC.2019.8722121
5. M. Q. Mao, C. Qian, Y. Ding, Decentralized coordination power control for islanding microgrid based on PV/BES-VSG, *CPSS Trans. Power Electron. Appl.*, **3** (2018), 14–24. https://doi.org/10.24295/CPSSTPEA.2018.00002

6. W. H. Wu, Y. D. Chen, L. M. Zhou, A. Luo, X. Zhou, Z. He, et al., Sequence impedance modeling and stability comparative analysis of voltage-controlled VSGs and current-controlled VSGs, *IEEE Trans. Ind. Electron.*, **66** (2018), 6460–6472. https://doi.org/10.1109/TIE.2018.2873523
7. K. Shi, H. H. Ye, W. T. Song, G. L. Zhou, Virtual inertia control strategy in microgrid based on virtual synchronous generator technology, *IEEE Access*, **6** (2018), 27949–27957. https://doi.org/10.1109/access.2018.2839737
8. H. S. Hlaing, J. Liu, Y. Miura, H. Bevrani, T. Ise, Enhanced performance of a stand-alone gas-engine generator using virtual synchronous generator and energy storage system, *IEEE Access*, **7** (2019), 176960–176970. https://doi.org/10.1109/ACCESS.2019.2957890
9. S. Saadatmand, M. Nia, P. Shamsi, M. Ferdowsi, D. C. Wunsch, Neural network predictive controller for grid-connected virtual synchronous generator, in *2019 North American Power Symposium (NAPS)*, IEEE, (2019), 1–6. https://doi.org/10.1109/NAPS46351.2019.900038
10. L. M. A Torres, L. A. C Lopes, T. L. A. Miguel, C. J. R. Espinoza, Self-tuning virtual synchronous machine: A control strategy for energy storage systems to support dynamic frequency control, *IEEE Trans. Energy Convers.*, **29** (2014), 833–840. https://doi.org/10.1109/TEC.2014.2362577
11. M. Guan, W. Pan, J. Zhang, Q. Hao, J. Cheng, X. Zheng, Synchronous generator emulation control strategy for voltage source converter (VSC) stations, *IEEE Trans. Power Syst.*, **30** (2015), 3093–3101. https://doi.org/10.1109/TPWRS.2014.2384498
12. H. Wu, X. B. Ruan, D. Yang, X. Chen, W. Zhao, Z. Lv, et al., Small-signal modeling and parameters design for virtual synchronous generators, *IEEE Trans. Ind. Electron.*, **63** (2016), 4292–4303. https://doi.org/10.1109/TIE.2016.2543181
13. H. Xu, X. Zhang, F. Liu, Virtual synchronous generator control strategy based on lead-lag link virtual inertia, *Proc. CSEE*, **37** (2017), 1918–1926. https://doi.org/10.13334/j.0258-8013.pcsee.160205
14. J. Liu, Y. Miura, T. Ise, Comparison of dynamic characteristics between virtual synchronous generator and droop control in inverter-based distributed generators, *IEEE Trans. Power Electron.*, **31** (2015), 3600–3611. https://doi.org/10.1109/TPEL.2015.2465852
15. K. Shi, H. Ye, P. Xu, D. Zhao, L. Jiao, Low-voltage ride through control strategy of virtual synchronous generator based on the analysis of excitation state, *IET Gener. Transm. Distrib.*, **12** (2018), 2165–2172. https://doi.org/10.1049/iet-gtd.2017.1988
16. J. Li, B. Wen, H. Wang, Adaptive virtual inertia control strategy of VSG for micro-grid based on improved bang-bang control strategy, *IEEE Access*, **7** (2019), 39509–39514. https://doi.org/10.1109/ACCESS.2019.2904943
17. J. W. Ding, J. B. Zhang, Z. H. Ma, VSG inertia and damping coefficient adaptive control, in *2020 Asia Energy and Electrical Engineering Symposium (AEEES)*, IEEE, (2020), 431–435. https://doi.org/10.1109/AEEES48850.2020.9121526
18. J. Alipoor, Y. Miura, T. Ise, Power system stabilization using virtual synchronous generator with alternating moment of inertia, *IEEE J. Emerging Sel. Top. Power Electron.*, **3** (2015), 451–458. https://doi.org/10.1109/JESTPE.2014.2362530
19. H. Z. Xu, X. Zhang, F. Liu, Control strategy of virtual synchronous generator based on differential compensation virtual inertia, *Autom. Electr. Power Syst.*, **41** (2017), 96–102. https://doi.org/10.7500/AEPS20160420001

20. M. X. Li, Y. Wang, N. Y. Xu, Virtual synchronous generator control strategy based on bandpass damping power feedback, *Trans. China Electrotech. Soc.*, **33** (2018), 2176–2185. https://doi.org/10.19595/j.cnki.1000-6753.tces.170201
21. X. Li, G. Chen, M. Ali, Improved virtual synchronous generator with transient damping link and its seamless transfer control for cascaded H-bridge multilevel converter-based energy storage system, *IET Electr. Power Appl.*, **13** (2019), 1535–1543. https://doi.org/10.1049/iet-epa.2018.5722
22. C. Li, Y. Q. Yang, N. Mijatovic, T. Dragicevic, Frequency stability assessment of grid-forming VSG in framework of MPME with feedforward decoupling control strategy, *IEEE Trans. Ind. Electron.*, **69** (2022), 6903–6913. https://doi.org/10.1109/TIE.2021.3099236
23. H. Xu, C. Yu, C. Liu, Q Wang, X. Zhang, An improved virtual inertia algorithm of virtual synchronous generator, *J. Mod. Power Syst. Clean Energy*, **8** (2019), 377–386. https://doi.org/10.35833/MPCE.2018.000472
24. Z. Lv, W. Sheng, H. Liu, L. Sun, M. Wu, Application and challenge of virtual synchronous machine technology in power system, in *Proceedings of the CSEE*, **37** (2017), 349–359. https://doi.org/10.13334/j.0258-8013.pcsee.161604
25. K. Shi, G. Zhou, P. Xu, H. Ye, F. Tan, The integrated switching control strategy for grid-connected and islanding operation of micro-grid inverters based on a virtual synchronous generator, *Energies*, **11** (2018), 1–20. https://doi.org/10.3390/en11061544
26. J. He, Y. W. Li, J. M Guerrero, F. Blaabjerg, J. C. Vasquez, An islanding microgrid power sharing approach using enhanced virtual impedance control scheme, *IEEE Trans. Power Electron.*, **28** (2013), 5272–5282. https://doi.org/10.1109/TPEL.2013.2243757
27. D. Chen, Y. Xu, A. Q. Huang, Integration of DC microgrids as virtual synchronous machines into the AC grid, *IEEE Trans. Ind. Electron.*, **64** (2017), 7455–7466. https://doi.org/10.1109/TIE.2017.2674621
28. Y. C. Zhu, M. F. Peng, X. Yu, Research on improved virtual synchronous generator based on differential compensation link, in *2018 IEEE 3rd International Conference on Integrated Circuits and Microsystems (ICICM)*, (2018), 259–263. https://doi.org/10.1109/ICAM.2018.8596677

AIMS Press